



Article

Solar Cells with Laser Doped Boron Layers from Atmospheric Pressure Chemical Vapor Deposition

Renate Zapf-Gottwick ^{1,*}, Sven Seren ², Susana Fernandez-Robledo ¹, Evariste-Pasky Wete ¹, Matteo Schiliro ¹, Mohamed Hassan ¹, Valentin Mihailetchi ³, Thomas Buck ³, Radovan Kopecek ³, Jürgen Köhler ¹ and Jürgen Heinz Werner ¹

¹ Institute of Photovoltaics and Research Center SCoPE, University of Stuttgart, Pfaffenwaldring 47, 70569 Stuttgart, Germany; susana.fdez.robledo@gmail.com (S.F.-R.); evariste-pasky.wete@ipv.uni-stuttgart.de (E.-P.W.); matteo.schiliro@ipv.uni-stuttgart.de (M.S.); mohamed.hassan@ipv.uni-stuttgart.de (M.H.); jr_koehler@gmx.de (J.K.); juergen.werner@ipv.uni-stuttgart.de (J.H.W.)

² SCHMID Group, Robert-Bosch-Straße 32-36, 72250 Freudenstadt, Germany; seren.sv@schmid-group.com

³ International Research Center Konstanz, Rudolf-Diesel-Straße 15, 78467 Konstanz, Germany; valentin.mihailetchi@isc-konstanz.de (V.M.); thomas.buck@isc-konstanz.de (T.B.); radovan.kopecek@isc-konstanz.de (R.K.)

* Correspondence: reate.zapf-gottwick@ipv.uni-stuttgart.de

Abstract: We present laser-doped interdigitated back contact (IBC) solar cells with efficiencies of 23% on an area of 244 cm² metallized by a screen-printed silver paste. Local laser doping is especially suited for processing IBC cells where a multitude of pn-junctions and base contacts lay side by side. The one-sided deposition of boron-doped precursor layers by atmospheric pressure chemical vapor deposition (APCVD) is a cost-effective method for the production of IBC cells without masking processes. The properties of the laser-doped silicon strongly depend on the precursor's purity, thickness, and the total amount of boron dopants. Variations of the precursor in terms of thickness and boron content, and of the laser pulse energy density, can help to tailor the doping and sheet resistance. With saturation-current densities of 70 fA/cm² at sheet resistances of 60 Ohm/sq, we reached maximum efficiencies of 23% with a relatively simple, industrial process for bifacial IBC-cells, with 70% bifaciality measured on the module level. The APCVD-layers were deposited with an inline lab-type system and a metal transport belt and, therefore, may have been slightly contaminated, limiting the efficiencies when compared to thermal-diffused boron doping. The use of an industrial APCVD system with a quartz glass transport system would achieve even higher efficiencies.

Keywords: laser processing; laser doping; APCVD; emitter; silicon solar cell; IBC



Citation: Zapf-Gottwick, R.; Seren, S.; Fernandez-Robledo, S.; Wete, E.-P.; Schiliro, M.; Hassan, M.; Mihailetchi, V.; Buck, T.; Kopecek, R.; Köhler, J.; et al. Solar Cells with Laser Doped Boron Layers from Atmospheric Pressure Chemical Vapor Deposition. *Solar* **2022**, *2*, 274–292. <https://doi.org/10.3390/solar2020015>

Academic Editor: Marko Topic

Received: 22 February 2022

Accepted: 10 May 2022

Published: 17 May 2022

Publisher's Note: MDPI stays neutral with regard to jurisdictional claims in published maps and institutional affiliations.



Copyright: © 2022 by the authors. Licensee MDPI, Basel, Switzerland. This article is an open access article distributed under the terms and conditions of the Creative Commons Attribution (CC BY) license (<https://creativecommons.org/licenses/by/4.0/>).

1. Introduction

Commercial photovoltaic (PV) modules comprising interdigitated back-contacted solar cells (IBC) still provide the highest efficiency. SUNPOWER Corp., with their Maxeon 3, offers PV modules with 112 half cells and an efficiency of 22.8% [1]. On the cell level, SUNPOWER's cells reached the 25% efficiency mark in the year 2014 with their standard IBC sequence on an area of 121 cm² [2]. They started early with their generation 1 to 3 cells on an area of around 155 cm² [3,4]. In the meantime, Kaneka achieved the highest cell efficiency of 26.6% on a designated area of around 179 cm² with their heterojunction technology on n-type IBC cells [5].

Most diffusion processes in photovoltaics occur via the thermal furnace diffusion of dopants. Without masking, the dopant atoms diffuse on the entire area of the front and rear side of the wafer, thus creating the quintessential pn-junction of solar cells. Unfortunately, using this type of furnace diffusion does not allow for locally doped regions, and thus requires expensive masking.

In general, local processing by laser irradiation is not only attractive for the cost-effective local doping of IBC cells [6,7], but also for other production steps of silicon solar cells. The laser ablation of thin dielectric layers is another one of these steps, e.g., for contact opening. Additionally, in conventional cells, laser doping for selective emitters [8,9] overcomes the difficulty in structuring the doped regions by masking processes. With a combination of the IBC structure and the concept of heterojunction solar cells, the upper theoretical limit for the conversion efficiency of IBC-silicon solar cells is approximately 29.1% [10].

On the cell level, we previously reported on laser-doped IBC cells with a 23.2% efficiency on a 4 cm² area [11]. Those cells used a sputtered boron oxide precursor. However, difficulties were experienced when upscaling the area of the cell in reaching a homogenous (with respect to thickness and boron-content) and clean deposition of the precursor for laser doping the pn-junction. Sputtering, at first sight, seems to be an attractive deposition method. However, in our experience, it presents two main difficulties for industrial applications, namely (i) the purity of the target, and (ii) the need for a (usually expensive) vacuum process. Therefore, we raised the question whether the APCVD deposition of boron-containing precursors would provide a viable alternative. Deposition via APCVD has the advantage of (i) pure gaseous precursors, and (ii) working under atmospheric pressure. So far, the deposition of boron-containing APCVD-layers has been used for precursors for thermal diffusion [12,13], mainly for co-diffusion processes for boron-diffusion on one side and phosphorus-diffusion on the other. For example, Heilig et al. [14] included APCVD-layers in a process for boron doping with a laser.

Here, we show that APCVD-deposited boron silicate glass (BSG) layers are well suited as precursor layers for laser doping p-type emitters on n-type wafers. The resultant doping depends strongly on the thickness as well as the boron content of the BSG. After the deposition of the BSG and before laser processing, an in situ deposited capping layer is necessary to prevent the boron oxide from creating boron acid due to humidity in air. In our study, we found undoped silicate glass (USG) to be superior to amorphous silicon. After the optimization of the APCVD deposition of the BSG and USG, laser processing produced several IBC-cells of industrial size with efficiencies of 23%. At present, the cell efficiency might be limited by impurities within the APCVD-deposited BSG and USG, which are probably due to the metallic conveyer of the APCVD lab-tool. Our reference cells with a furnace-diffused emitter had a 0.3% higher efficiency.

2. Materials and Methods

2.1. Solar Cells

In our experiments, we used commercially available Czochralski (Cz) grown n-type silicon wafers with a base resistivity $p \approx 1.5 \Omega\text{cm}$ and an (100)-oriented surface. The pseudo-square wafers of size M2 (edge length of the square is 156.7 mm) and an area of 244.3 cm² had a thickness of around 140 μm after texturing and polishing. The front side of the wafers used for solar cells was chemically textured with a potassium hydroxide and Alkatex solution to obtain random pyramids. The Alkatex solution was commercially available. The rear side of the wafers for solar cells and the test samples for lifetime were chemically polished, also with a potassium hydroxide solution at a temperature of 80 °C.

Figure 1 schematically shows the cross section of the Laser-IBC solar cells. After texturing the front and chemically polishing the back side, further processing began with the one-sided deposition of boron-containing precursor layers by APCVD: Borosilicate Glass (BSG) and the capping layer of Undoped Silicate Glass (USG). Then, local laser doping created the locally well-defined boron-doped emitters on the rear side of the wafer. Thus, the local pn-junctions formed. Then, hydrofluoric acid was used to clean the silicon surface of the remaining precursor. Subsequent RCA cleaning [15] removed impurities before furnace diffusion by phosphor oxychloride (POCl₃). This diffusion (in particular the P-content of the phosphorusoxide) was co-optimized for the next step of creating the lightly doped front surface field (FSF) [16] and the heavily laser-doped base contact (back

surface field, BSF). The P-containing BSF was also locally formed by laser doping between the B-emitter regions, using the furnace-deposited phosphorsilicate glass (PSG) as a P-source. Then, an HF-Dip was used to remove the rest of the PSG. A subsequent, tailored etch-back with a solution of hydrofluoric acid, nitric acid, and acetic acid uniformly etched the high surface concentration of phosphorus at the silicon surfaces at a depth of around 50 nm. This shallow etching step only removed a small fraction of the deep doping profile of the (more deeply laser-diffused) BSF as well as the boron-emitter, also increasing the parallel resistance of the finished cells. The texture on the front side was not affected, while the sheet resistance of the FSF increased slightly. Another RCA-step was employed to clean the sample before the next step of dry thermal oxidation. A double-layer stack consisting of a thermally grown 15 nm thick silicon dioxide (SiO_2) together with 65 nm thick plasma-enhanced chemical vapor-deposited silicon nitride ($\text{SiN}_x\text{:H}$) passivated the front and rear side. Finally, screen-printed, dried and fired silver paste came into contact with the emitter and BSF regions. The four busbars for each polarity were separately printed with a low-temperature, cured silver paste and were isolated to the contact fingers of opposite polarity via a printed and cured polymer paste. The metallization design resembles that of ZEBRA cells [17,18] and allows for bifacial illumination.

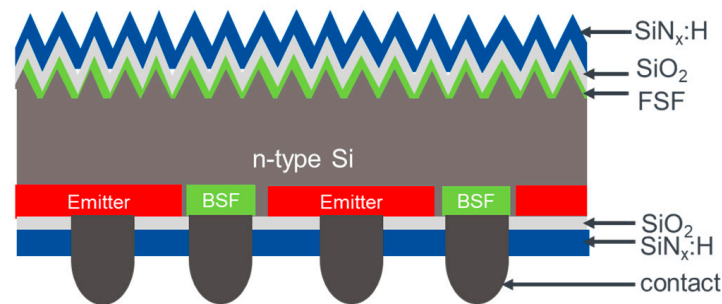


Figure 1. Schematic cross section of a Laser-IBC solar cell with textured front side and polished rear side. A double layer of silicon dioxide (SiO_2) and silicon nitride ($\text{SiN}_x\text{:H}$) passivates the surfaces. The rear side has multiple emitters and base contacts (BSF) laying side-by-side, also passivated by the stack SiO_2 and $\text{SiN}_x\text{:H}$. Screen-printed silver paste contacts both doped regions. Instead of thermal diffusion, emitter and BSF are doped by a laser process.

Current/voltage-measurements of the IBC cells were performed using a cell flasher from HALM, based on the Cetis PV-CT-L1 tool.

2.2. Structure of Test Samples

During solar-cell processing, we monitored different steps by measuring specifically designed test samples. The laser doping of boron out of the APCVD-layers was analyzed using control samples and by measuring the following aspects:

- Sheet resistance R_{sh} ;
- Lifetime τ ;
- Saturation current density J_0 ;
- Contact resistivity ρ_c .

Figure 2a shows a schematic cross section of the R_{sh} -sample, while the cross section of the τ -sample is presented in Figure 2b. After the deposition of the APCVD-layers BSG and USG, the laser irradiated the precursor with different laser pulse energy densities (see Section 2.3).

The passivation of the front and the rear side of lifetime samples consists of the same stack used in the passivation of solar cells (see Section 2.1). The R_{sh} -values were measured with a four-point-probe and checked using the Transfer Length method (TLM) at contact resistance samples, both methods used the set-up GP Solar GP 4-Test Pro. The lifetimes τ derived from a quasi-steady-state photo conductance measured with a Sinton WCT-120 that, in turn, yielded the saturation current density J_0 [19].

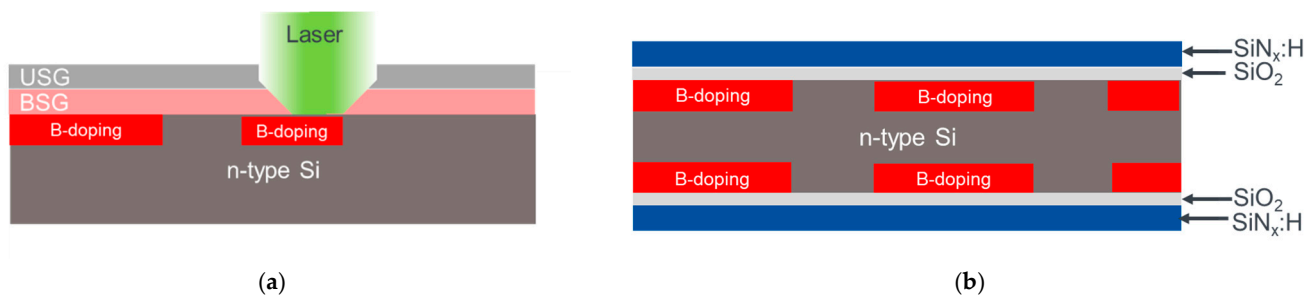


Figure 2. Schematic cross sections: (a) Test sample for measuring sheet resistances after laser doping. The boron diffuses by laser irradiation out of the precursor on top of silicon: Boron silicate glass (BSG) and undoped silicate glass (USG); (b) Test sample for measurements of the lifetime τ . The boron-doping is symmetrically done on the front and rear side, and then passivated by the bilayer stack of SiO_2 and $\text{SiN}_x\text{:H}$, the same as used for solar cells.

For the characterization of R_{sh} , the laser irradiated fields with an area of $1.5 \times 1.5 \text{ cm}^2$. Including one field without doping, there were 15 laser doped fields on the wafer with different laser parameters. For characterization of the lifetime τ , the laser irradiated eight fields symmetrically on both sides of the wafer with a size of $4.0 \times 4.0 \text{ cm}^2$, resulting in eight laser doped fields and one without laser doping. The contact resistivity was measured on fields irradiated by the laser with different laser pulse energy densities similar to the τ -samples in areas of $4.0 \times 4.0 \text{ cm}^2$. After passivation and metallization with the silver fingers (see Section 2.1) and cutting into strips of 1 cm width, TLM was used to measure the contact resistivity.

2.3. Laser Doping Set-Up

The setup for laser doping included a Q-switched frequency-doubled Nd:YAG laser with a wavelength $\lambda = 532 \text{ nm}$ and a pulsed laser beam with pulse duration τ_p between $41 \text{ ns} < \tau_p < 110 \text{ ns}$ at full-width-half-maximum intensity. Optics formed a quasi-line focus with a width of $12 \mu\text{m}$ in the x -direction and a length of $280 \mu\text{m}$ in the y -direction. The laser intensity I , along the short (x -)axis had a Gaussian distribution and a top-hat distribution along the long (y -)axis. The laser pulse energy density H_p was calculated according to Hassan et al. [20]. To dope large areas, the laser irradiated the sample by scanning in the x - and y -direction and by moving a table on which the sample was mounted. As a consequence, the laser pulses overlapped in the x -direction with O_x and in the y -direction with O_y . Both overlaps are represented as a percentage of the whole width of a single laser beam.

The laser doping itself relied on liquid-phase diffusion in the molten Si. On the one hand, the several-nanoseconds-long laser pulse led to the melting of the Si for about 100 ns. On the other hand, the laser pulse also evaporated the APCVD-deposited precursor. The resulting re-condensed vapor of the precursor served as the source for the doping process [20,21]. In molten Si, the dopants' diffusion coefficient was orders of magnitude higher compared to the solid state [22].

2.4. Deposition of APCVD-Layers

When compared to furnace diffusion, the APCVD process has the advantage of resulting only in a one-sided deposition. Additionally, deposition is possible without the evacuation of the process chamber. This leads to a more cost- and time-efficient process in comparison to sputtering or evaporation processes [23].

In our experiments, we used the APCVD-lab-tool "SierraTherm 5K6-130C56-13-BSG/PSG-SiTiO₂" from the company SCHMID. The wafers were transported by a metallic belt, first into a heating zone, then through three injection chambers and, finally, through a cooling zone. In contrast to the lab tool with a metallic belt, the industrial tools of

SCHMID use a belt with ceramic parts. Those metal-free industrial tools were not available to us at the time of our investigation.

In the first chamber, BSG deposition occurs by the injection of diborane (B_2H_6), silane (SiH_4) and oxygen (O_2) [24] gases and the following chemical reaction:



The B_2H_6 reacts with O_2 by



Chambers 1, 2 and 3 contained the same injection heads, whereas chambers 2 and 3 were used for the deposition of undoped silicate glass (USG) by the reaction of the gases SiH_4 and O_2 . The effective wafer temperature was 360 °C for the deposition of BSG and around 400 °C for USG. The purity of the gases was around 5 N. The concentration of boron in BSG was controlled by the injection of 5% diborane in hydrogen and silane and the ratio of these gases. All of the boron from the gas was incorporated into the BSG-layer, as confirmed by glow discharge optical mass spectrometry. Ellipsometry measurements were used to control the thickness of the layer.

Unfortunately, the transportation belt of the lab-type APCVD reactor is made out of metal, which provides advantages in terms of the versatility of the system to deposit, alongside doped glasses, TiO_2 , AlO_x , and in situ doped aSi/polySi. Industrial-type transport systems for the wafers use pure ceramic rolls. In order to avoid the metal contamination of wafers and the APCVD-layers using the metal belt system, we tested different support wafers in the experiments, which served not only as wafer carriers but also as diffusion barriers between the metallic belt and the solar cell wafers (see Sections 3.2 and 3.4). At the deposition temperatures used, metals out of the belt were able to diffuse into the solar cell wafers and also into the APCVD-layers. To minimize possible contamination further, the metal belt was coated with BSG and USG for several hours to build an even more effective diffusion barrier. Nevertheless, when using the metal belt, contamination of the APCVD-layers cannot be avoided completely. Therefore, we tested different support wafers as diffusion barriers between the belt and the test samples (see Section 3.2). For each deposition run, we used cleaned support wafers, that had been partly used multiple times, for deposition on both sides of the wafers. Dipping with hydrofluoric acid directly before deposition as well as RCA cleaning ensured that the Si surface of the test samples was clean before being sent to SCHMID. The wafers were exchanged between *ipv* and SCHMID by mail via nitrogen-containing packages.

3. Results

In the following Section, we show that the APCVD-layers are well suited for laser doping the pn-junction for solar cells and—despite the metal conveyer in the APCVD system—we reached efficiencies of above 22.5% with a maximal value of 23%. For this purpose, we compared the following three different processes for fabricating the pn-junctions on the n-type solar cell wafers: (i) laser doping via *sputtered* boron oxide layers leading to 23.2% [11], (ii) laser doping via *APCVD-layers*, and (iii) *furnace* diffusion of boron by boron tribromide (BBr_3) yielding 23.3% efficient cells.

3.1. Laser Doping and Sheet Resistance

The success of laser doping of Si highly depends on the composition of the precursor. The BSG layers tested here with capping layers of either USG or aSi are characterized as follows:

- Boron concentration C_B within the BSG;
- Thickness d_{BSG} of the BSG;
- Thickness d_{USG} of the capping layer USG, or d_{aSi} of aSi.

The capping layer of either aSi or USG prevents the chemical reaction of B_2O_3 with humidity (from the air) to boric acid.

The measured sheet resistance R_{sh} of the boron-doped layers was used to investigate the correlation of the laser irradiation and the composition of the layers as a function of the laser pulse energy density H_p and laser pulse overlap O .

3.1.1. Laser Pulse Overlap

The pulse energy density H_p of the laser changes the melting depth of the Si, while the overlap O , controls the doping profile [20]. Therefore, the sheet resistance as well as the doping profile can be tailored with proper laser parameters [20–22].

Figure 3a shows the optimization of the overlap O_x for $29\% < O_x < 79\%$ while the overlap in the y-direction O_y remains constant $O_y = 12.5\%$. The APCVD layers for these experiments consisted of a BSG layer of a thickness of $d_{BSG} = 40$ nm with 12% boron and a USG layer of a thickness of $d_{USG} = 20$ nm. At $75\% < O_x < 79\%$, the sheet resistance R_{sh} leveled off at $R_{sh,min} \approx 70 \Omega/sq$. Figure 3b shows the resulting R_{sh} with a variation of O_y in the range $9\% < O_y < 36\%$. For the variation, we increased the thickness of USG to $d_{USG} = 40$ nm and decreased the boron concentration in BSG to $C_B = 8\%$. Only the value of $O_y \leq 9\%$ seemed to influence R_{sh} at different laser-pulse-energy densities H_p . With these results, we proceeded with $O_x = 75\%$ and $O_y = 13\%$ as the standard for further laser doping.

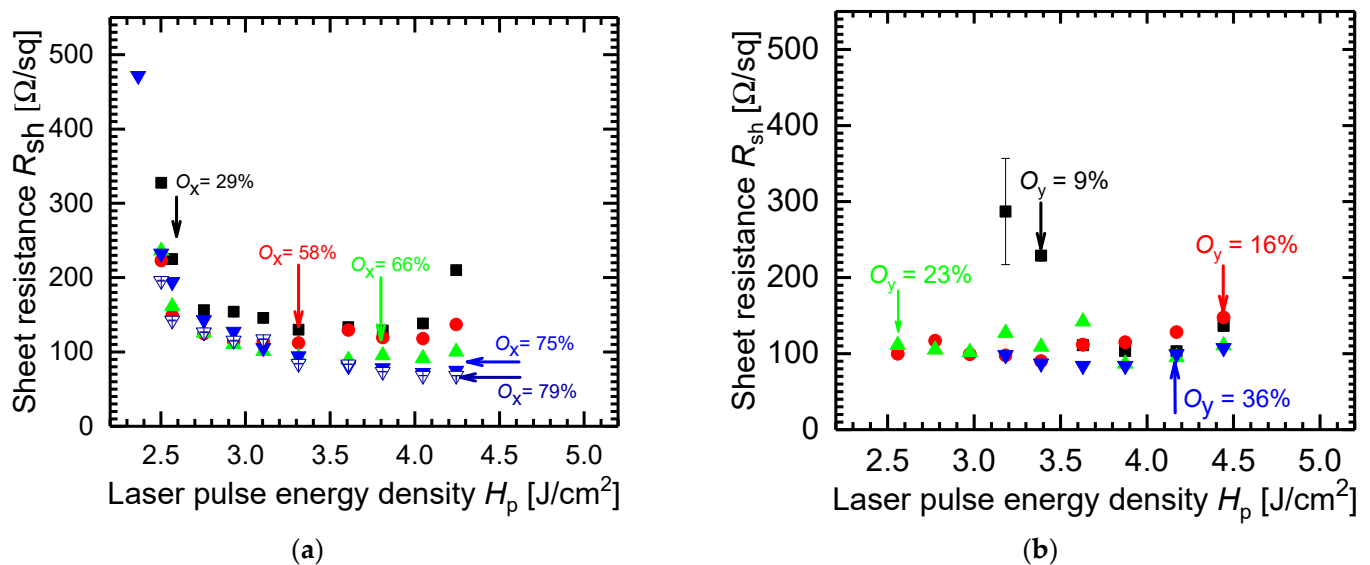


Figure 3. Sheet resistance R_{sh} after laser doping from APCVD-layers with (a) 12% boron in BSG, and a thickness $d_{BSG} = 40$ nm, USG thickness $d_{USG} = 20$ nm. Pulse overlaps $75\% < O_x < 79\%$ in x-direction of the laser reduce and stabilize R_{sh} at $R_{sh,min} \approx 70 \Omega/sq$ for a constant overlap $O_y = 12.5\%$ in y-direction. (b) 8% boron in BSG, $d_{BSG} = 40$ nm, $d_{USG} = 40$ nm. The value of R_{sh} is stable for an overlap $O_y > 9\%$ in y-direction at constant $O_x = 75\%$.

3.1.2. Boron Concentration

The boron concentration C_B in the BSG controls the maximum possible doping concentration $C_{B,em}$ of the p-type layer of the pn-junction. For our APCVD parameters, the maximal possible B-concentration in the BSG was $C_B = 12\%$. We used $C_{B,1} = 4.5\%$, $C_{B,2} = 8\%$, and $C_{B,3} = 12\%$ for $d_{BSG} = 40$ nm and $d_{USG} = 20$ nm for different laser-pulse-energy densities H_p .

Figure 4a shows the R_{sh} after laser doping of APCVD-layers with a BSG of thickness $d_{BSG} = 40$ nm and USG with $d_{USG} = 20$ nm. Stable and leveled-off sheet resistances $R_{sh} \approx 80 \Omega/sq$ were reached between $3 J/cm^2 < H_p < 4 J/cm^2$ for a boron concentration of $C_{B,3} = 12\%$ of the APCVD layers. The lower $C_{B,2} = 8\%$ required a higher H_p for the same R_{sh} , while $C_{B,1} = 4.5\%$ did not result in stable R_{sh} . We found that the higher the C_B , the

lower the threshold in H_p for a given value in R_{sh} . This correlation is shown in Figure 4b where—instead of R_{sh} —the equivalent sheet conductance $G_{sh} = 1/R_{sh}$ is plotted. Laser doping requires laser energies H_p of above the melting threshold $H_{p,thres}$ of the Si [20]. The doping threshold was observed via an increase in the sheet conductance in Figure 4b. Due to the partial absorption of the laser power within the APCVD-layer, the measured threshold was found to be dependent on the boron content of the precursor layer. With $H_{p,thres,3}$ (12%) = 2.1 J/cm² in Figure 4b, the threshold energy $H_{p,thres}$ for laser doping with $C_{B,3} = 12\%$ was found to be lower than $H_{p,thres,2}$ (8%) = 2.6 J/cm² for $C_{B,2} = 8\%$. This is discussed in more detail below.

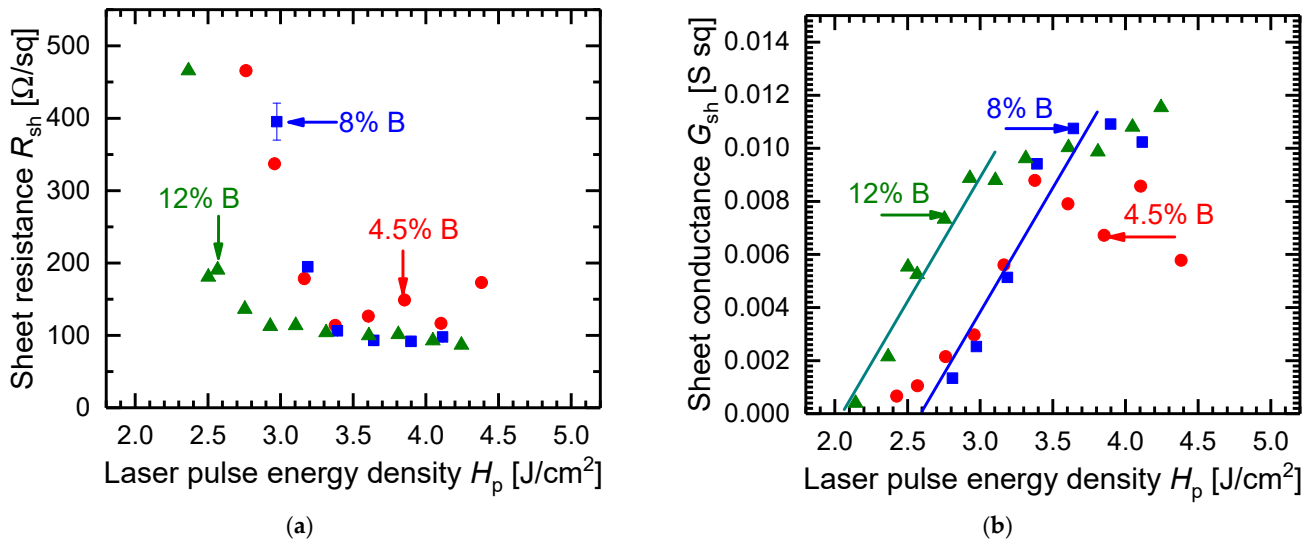


Figure 4. Laser doping from APCVD-layer with BSG of thickness $d_{BSG} = 40$ nm and USG with $d_{USG} = 20$ nm. (a) Sheet resistance levels off at $R_{sh} \approx 80$ Ω/sq for $3 \text{ J/cm}^2 < H_p < 4 \text{ J/cm}^2$ for boron concentration $C_{B,3} = 12\%$. For $C_{B,2} = 8\%$ one needs higher H_p for the same R_{sh} , while $C_{B,1} = 4.5\%$ does not lead to really predictable R_{sh} . (b) Using a sheet conductance of $G_{sh} = 1/R_{sh}$ to deduce threshold values for the pulse energy densities: $H_{p,thres,3} = 2.1 \text{ J/cm}^2$ for $C_{B,3} = 12\%$ and $H_{p,thres,2} = 2.6 \text{ J/cm}^2$ with $C_{B,2} = 8\%$. Measurement error in R_{sh} is somewhat smaller than size of symbols. The lines drawn for $C_{B,2} = 8\%$ and $C_{B,3} = 12\%$ are guides to the eye.

3.1.3. Variation of Capping Layer

The APCVD equipment provided the opportunity to deposit, as the capping layer, amorphous Si (aSi) instead of USG. Hence, we compared the laser doping from BSG with different capping layers of USG with thicknesses of (i) $d_{USG,1} = 20$ nm and (ii) $d_{USG,2} = 40$ nm, and finally, also with aSi capping (iii) with a thickness of $d_{aSi} = 30$ nm. The BSG had a boron concentration of $C_B = 12\%$ and a thickness of $d_{BSG} = 40$ nm.

Figure 5a shows the sheet resistances R_{sh} after laser doping. The main result is that the thickness of the USG did not influence R_{sh} at $H_p < 3.3 \text{ J/cm}^2$; therefore, the thicker the USG, the higher the R_{sh} at $H_p > 3.3 \text{ J/cm}^2$. The aSi capping layer yielded the lowest R_{sh} . With the sheet conductance values in Figure 5b, we can derive the threshold values $H_{p,thres}$ for the laser doping. The $H_{p,thres}$ are about the same for $d_{USG,1} = 20$ nm and $d_{USG,2} = 40$ nm, whereas they are higher for the aSi-capping $H_{p,thres,aSi} > H_{p,thres,USG}$. The lower band gap of the aSi layer absorbs more laser radiation than the USG. Therefore, it required more power to melt the underlying Si and to evaporate the BSG layer.

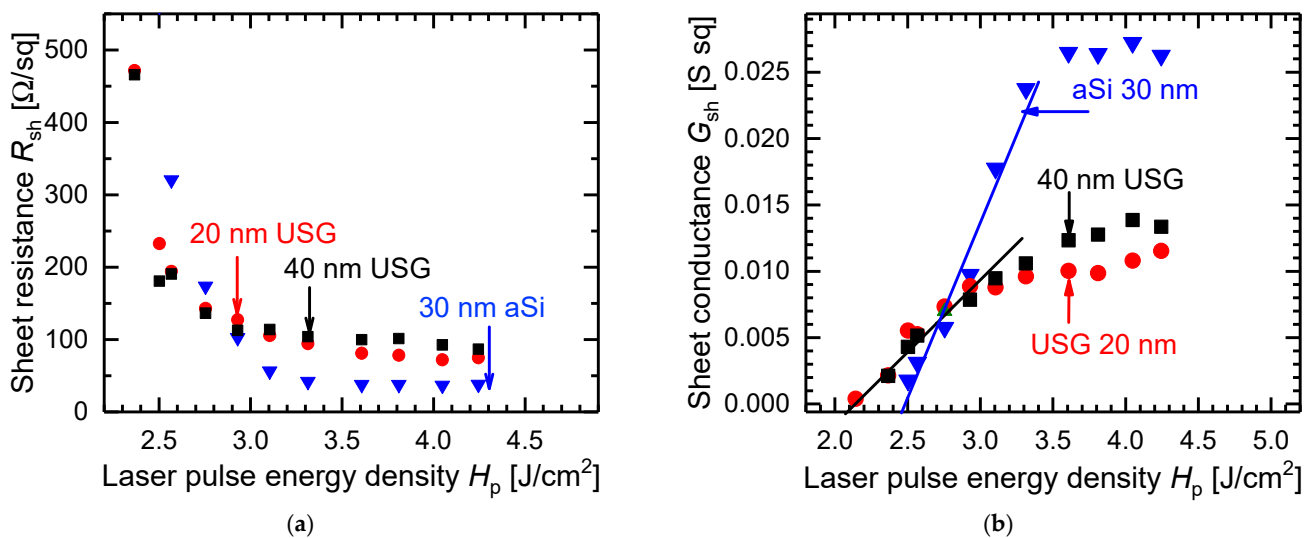


Figure 5. Laser doping with different laser pulse energy densities H_p for APCVD-layers with BSG thickness of $d_{BSG} = 40$ nm and boron concentration of $C_B = 12\%$. (a) Stable sheet resistances R_{sh} for $H_p > 3$ J/cm². The thickness $d_{USG,1} = 20$ nm of USG yields slightly lower R_{sh} than for $d_{USG,2} = 40$ nm. Lowest R_{sh} reached with the aSi capping layer of thickness $d_{aSi} = 30$ nm. (b) Applying the sheet conductance $G_{sh} = 1/R_{sh}$ shows that the threshold $H_{p,thres}$ at $G_{sh} = 1$ Ssq is about the same for laser doping with USG with $d_{USG,1} = 20$ nm and $d_{USG,2} = 40$ nm. In contrast, $H_{p,thres,aSi}$ for aSi is higher. The measurement error of R_{sh} is somewhat smaller than the size of the symbols used. Lines are guides to the eye.

At first sight, the aSi capping layer seems more attractive than USG. However, the aSi capping layers lead to a severe processing problem, in that after the laser doping, the surface cannot be cleaned completely, as shown in Figure 6. Neither cleaning with a KOH solution nor with a solution of hydrofluoric acid, nitric acid, and acidic acid results in clean surfaces without rests or glitters. Therefore, we did not continue experiments with aSi capping layers. However, as the deposited aSi layers were in situ boron-doped, a BRL (boron rich layer) could have been formed during laser processing, complicating and partially preventing etching.

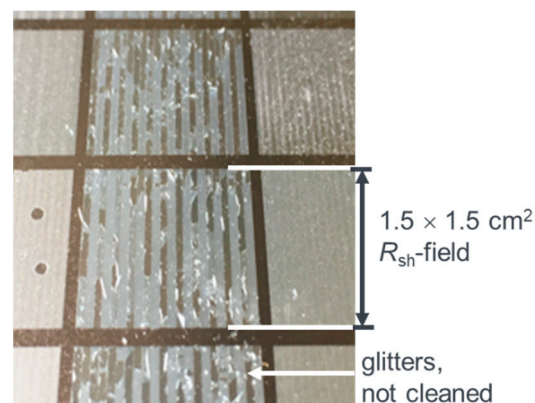


Figure 6. Photo of R_{sh} -fields after laser doping and cleaning; an aSi capping layer on BSG is used before the laser process. Wet chemical cleaning does not lead to clean surfaces without rests and glitters of aSi.

3.1.4. Thickness of BSG

For a fixed boron content in the capping layer, different thicknesses led to the following two effects: on the one hand, the thicker the layer, the more boron atoms available for laser

doping. As a result, the final doping concentration in the boron emitter of the solar cell increased. On the other hand, thicker BSG layers led to a stronger absorption of the laser beam. Therefore, more power is needed to melt the underlying Si for doping. The required threshold value was higher. In our experiments, we varied the BSG thickness d_{BSG} in the range of $20 \text{ nm} < d_{\text{BSG}} < 120 \text{ nm}$, while the boron concentration $C_{\text{B}} = 12\%$ and the thickness $d_{\text{USG}} = 40 \text{ nm}$ of the USG capping layer remained constant.

Figure 7a shows R_{sh} after laser doping with different laser-pulse-energy densities H_{p} . The R_{sh} values are about the same for BSG with $d_{\text{BSG},1} = 20 \text{ nm}$ and $d_{\text{BSG},2} = 40 \text{ nm}$. In contrast, $d_{\text{BSG},3} = 80 \text{ nm}$ and $d_{\text{BSG},4} = 120 \text{ nm}$ require higher H_{p} . Figure 7b allows us to deduce the threshold values for laser doping from the values for $G_{\text{sh}} \rightarrow 0 \text{ S sq}$. These threshold values $H_{\text{p,thres}}$ increase with the thickness d_{BSG} of the BSG-layer and are:

- $H_{\text{p,thres},1} = 2.4 \text{ J/cm}^2$ for $d_{\text{BSG},1} = 20 \text{ nm}$;
- $H_{\text{p,thres},2} = 2.45 \text{ J/cm}^2$ for $d_{\text{BSG},2} = 40 \text{ nm}$;
- $H_{\text{p,thres},3} = 2.9 \text{ J/cm}^2$ for $d_{\text{BSG},3} = 80 \text{ nm}$;
- $H_{\text{p,thres},4} = 3.2 \text{ J/cm}^2$ for $d_{\text{BSG},4} = 120 \text{ nm}$.

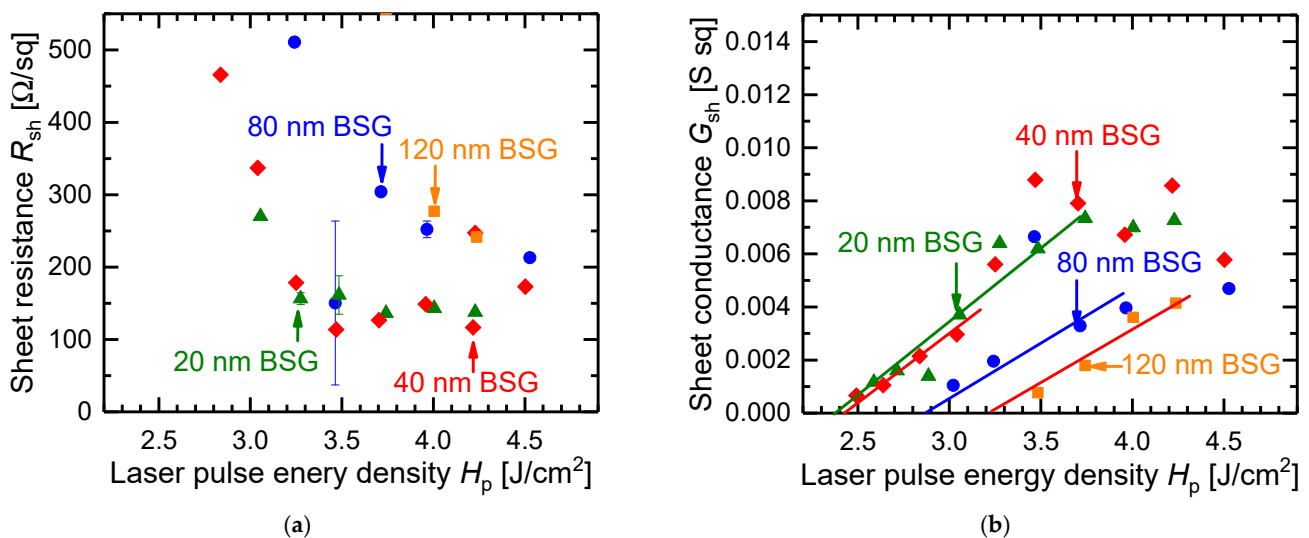


Figure 7. Laser doping with different laser pulse energy densities H_{p} for APCVD-layers with BSG of thickness $20 \text{ nm} < d_{\text{BSG}} < 120 \text{ nm}$ and boron concentration $C_{\text{B}} = 12\%$ and USG with $d_{\text{USG}} = 40 \text{ nm}$. (a) Same sheet resistances R_{sh} for laser doped BSG with $d_{\text{BSG},1} = 20 \text{ nm}$ and $d_{\text{BSG},2} = 40 \text{ nm}$ while higher d_{BSG} needs higher H_{p} . (b) The plot with the sheet conductance G_{sh} reveals a higher threshold value for higher d_{BSG} .

3.1.5. Homogeneity of APCVD-Layers

To obtain more information about the homogeneity of laser-doped pn-junctions for solar cells on the area of M2-wafers, we laser-irradiate the full area of the Si wafers with BSG/USG on top with one laser pulse energy density, of $H_{\text{p}} = 3.6 \text{ J/cm}^2$. The key parameter for the laser doping of thin layers is the thickness of the layer and the content of the doping material. The R_{sh} measurements were performed on 81 points, evenly distributed over the wafer.

Figure 8a shows the color contour plot of R_{sh} after laser doping of the APCVD-layer with BSG of thickness $d_{\text{BSG}} = 40 \text{ nm}$ and boron concentration $C_{\text{B}} = 12\%$ and USG with a thickness $d_{\text{USG}} = 20 \text{ nm}$. The mean value is $R_{\text{sh,mean}} = 59 \text{ Ω/sq}$ with a difference of $\Delta R_{\text{sh}} = 10 \text{ Ω/sq}$ between the maximal and minimal value. After laser doping the pn-junction for solar cell processing, phosphorus diffusion occurred for the BSF field and the growth of thermal silicon dioxide (for the surface passivation). Figure 8b displays the changed R_{sh} . We obtained a mean value of $R_{\text{sh,mean,ox}} = 69 \text{ Ω/sq}$ and a deviation of $\Delta R_{\text{sh,ox}} = 20 \text{ Ω/sq}$. The etchback after P-diffusion and oxidation increased the R_{sh} .

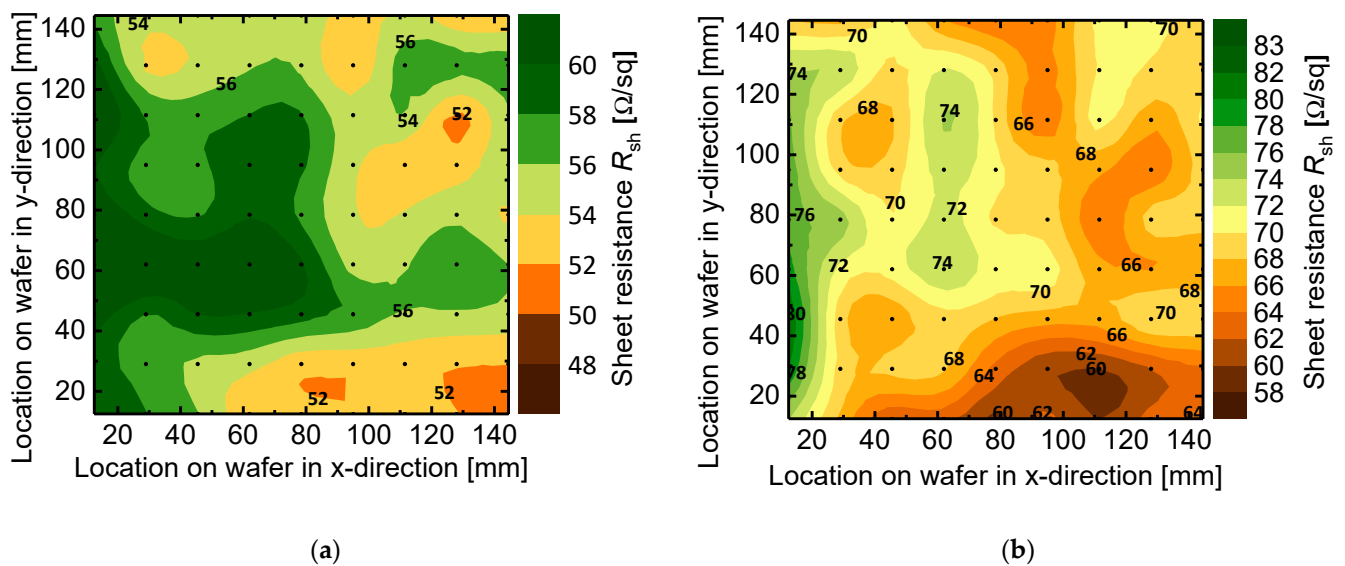


Figure 8. Color contour plot of sheet resistance R_{sh} after boron laser doping with constant laser pulse energy density $H_p = 3.6 \text{ J/cm}^2$ on a Si wafer. The R_{sh} -homogeneity is tested for APCVD-layers with $d_{BSG} = 40 \text{ nm}$, $C_B = 12\%$, and USG with a thickness $d_{USG} = 20 \text{ nm}$. (a) Directly after laser doping with a deviation ΔR_{sh} (from the maximal to minimal value) in R_{sh} of $\Delta R_{sh} \approx 10 \text{ } \Omega/\text{sq}$ and, (b) after boron laser doping, phosphorus diffusion and oxidation with $\Delta R_{sh,ox} \approx 20 \text{ } \Omega/\text{sq}$. The four-point-probe measurements of R_{sh} are only feasible 10 mm apart from the edges of the wafer.

3.1.6. Stability of APCVD-Layers

Figure 9 shows the stability of the APCVD layers for laser doping. The layers consisted of BSG with a thickness of $d_{BSG} = 40 \text{ nm}$, a boron concentration of $C_B = 12\%$, and USG of $d_{USG} = 20 \text{ nm}$. Four laser-doping experiments were performed over the course of 21 days in order to investigate the effect of storing the APCVD layers before the laser-doping process. Before laser doping, the wafers with the layers were stored in a nitrogen atmosphere to protect them from air humidity. Only a minimal variation in the range of $10 \text{ } \Omega/\text{sq} < \Delta R_{sh} < 15 \text{ } \Omega/\text{sq}$ was observed within this time.

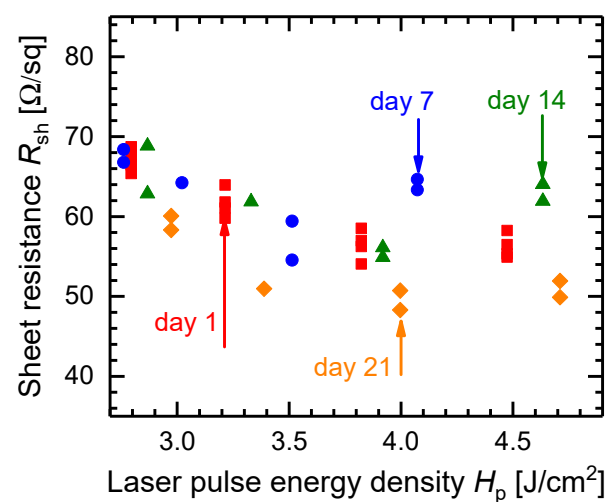


Figure 9. Stability test of APCVD-layers. Before laser doping the wafers with the layers are stored between 1 and up to 21 days in a nitrogen atmosphere to protect them from air humidity. The sheet resistances R_{sh} serves as a measure for stability for the four different storage times. The maximum difference ΔR_{sh} between the experiments over the three weeks, in ranges of $10 \text{ } \Omega/\text{sq} < \Delta R_{sh} < 15 \text{ } \Omega/\text{sq}$.

3.2. Saturation Current Densities

During deposition of the APCVD-layers, the wafers were transported on support wafers to avoid possible contamination from the metallic belt of the conveyer. As support wafers, we used M2-sized Cz-Si wafers with a texture on both sides. The APCVD layers consisted of BSG with a thickness of $d_{BSG} = 40$ nm, a boron concentration of $C_B = 12\%$, and USG with $d_{USG} = 20$ nm. The sheet resistance varied due to different laser-pulse-energy densities.

We tested the following support/diffusion barrier wafers (SW) between the metal belt and the process wafers:

- Unperforated wafers with 200 nm thick SiN deposited on both sides;
- Perforated wafers to avoid floating of the wafers during APCVD depositions (“perforation” means small holes in the wafer);
- Unperforated wafers.

To understand its influence on the purity of the APCVD-layers, we measure the effective lifetime τ_{eff} and extracted the saturation current density $J_{0,E}$ after laser doping and the passivation of the surface (see Section 2.2). The corrections of τ_{eff} due to Auger- and radiative recombination in the bulk in the form of the intrinsic lifetime τ_{intr} and the injection-corrected intrinsic-carrier density $n_{i,eff}$ were included in the software of the WCT-120 tool. The Auger- and radiative corrected lifetime τ_{corr} can be described by

$$\frac{1}{\tau_{corr}} = \frac{1}{\tau_{eff}} - \frac{1}{\tau_{intr}} = J_{0,E} \frac{N_b + \Delta n}{qwn_{i,eff}^2} \quad (3)$$

showing the influence of the bulk doping N_b , the concentration of injected charge carriers Δn , the width w of the sample, and the elementary charge q [25,26]. When measuring τ_{eff} at a high injection, the lowly doped base enters into high-injection, while the highly doped emitter remains in low-injection. In the high-injection state, the Shockley–Read–Hall (SRH) lifetime of the bulk Si is assumed to be higher than τ_{intr} and higher than the lifetime in the highly doped emitter or not injection dependent [27,28]. From the derivative of $1/\tau_{corr}$ with respect to Δn , we were then able to extract the $J_{0,E}$ via the following equation

$$\frac{d}{d\Delta n} \left(\frac{1}{\tau_{corr}} \right) = \frac{2J_{0,E}}{qw n_{i,eff}^2} \quad (4)$$

As result, Figure 10 shows the $J_{0,E}$ for the case of using the support wafers during APCVD-deposition. The lowest $J_{0,E}$ is reached with the support wafers (SW) without perforation and with SiN. Unfortunately, the deposition with the SW with perforation exhibits only one value of $J_{0,E} = 110$ fA/cm², the highest $J_{0,E}$ of all. Metallic impurities from the transport belt probably reached the process wafers via the holes in the SW. The $J_{0,E}$ with deposition on SWs without perforation ranges from 58 to 94 fA/cm². Only the deposition on SWs without perforation and with SiN resulted in a decreasing $J_{0,E}$ with increasing R_{sh} (lower doping); with the lowest $J_{0,E} = 40$ fA/cm² at $R_{sh} = 104$ Ω/sq. Only the $J_{0,E}$ of the test samples with the deposition on SW without perforation and with SiN show a dependence on R_{sh} . The decrease in $J_{0,E}$ with increasing R_{sh} suggests that lifetime is limited more or less by the Auger-recombination in the emitter and not by contaminations or defects. The lifetime due to Auger-recombination should show a dependence on the inverse of the square of the charge carrier concentration of the highly doped emitter [29] or, in other words, it should increase with R_{sh}^2 or vice versa to $J_{0,E}$.

If the APCVD-process contaminated the BSG/USG-layer, the laser doping would bring the contamination into the emitter within a depth of around 1 μm [20]. The etch-back following P-diffusion (see Section 2.1) also ensures at least a partial removal of contaminants on the surface.

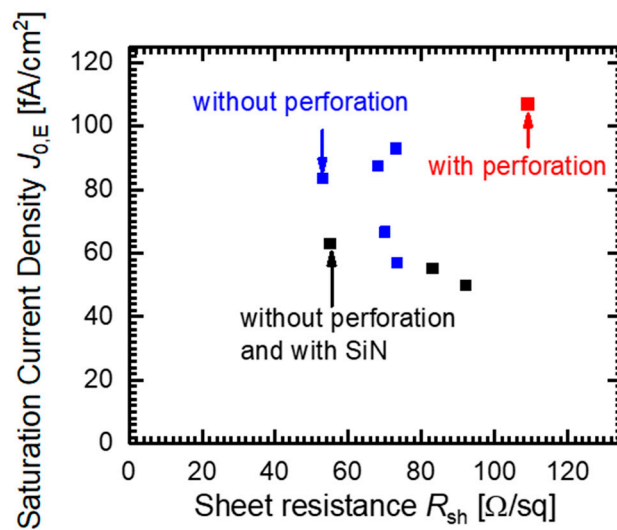


Figure 10. Saturation current density $J_{0,E}$ after laser doping and passivation. Different support wafers between the metal belt of the transport system and the process wafers are used during the deposition of the APCVD-layers. $J_{0,E}$ is lowest for the support wafers without perforation and with SiN on their surfaces showing a $J_{0,E}$ decreasing with the sheet resistance R_{sh} .

Parallel to the samples shown here for measuring lifetime/saturation current density, we processed solar cells with emitters from the deposition of APCVD layers with SW without perforation and with SiN and laser doping—see the following Section 3.4.

3.3. Contact Resistivity

High quality Ohmic contacts on the boron-containing laser-doped emitters of our cells required low contact resistances ρ_C to the screen-printed silver paste. Figure 11 shows the ρ_C of the fired Ag paste on the laser-doped APCVD layers. The ρ_C decreased with decreasing R_{sh} , with the lowest $\rho_C = 3 \text{ m}\Omega\text{cm}^2$ at $R_{sh} \approx 108 \text{ }\Omega/sq$. The APCVD-layers consist of BSG with a thickness of $d_{BSG} = 40 \text{ nm}$, a boron concentration of $C_B = 12\%$, and USG of $d_{USG} = 20 \text{ nm}$. Sheet resistance varied due to different laser-pulse-energy densities.

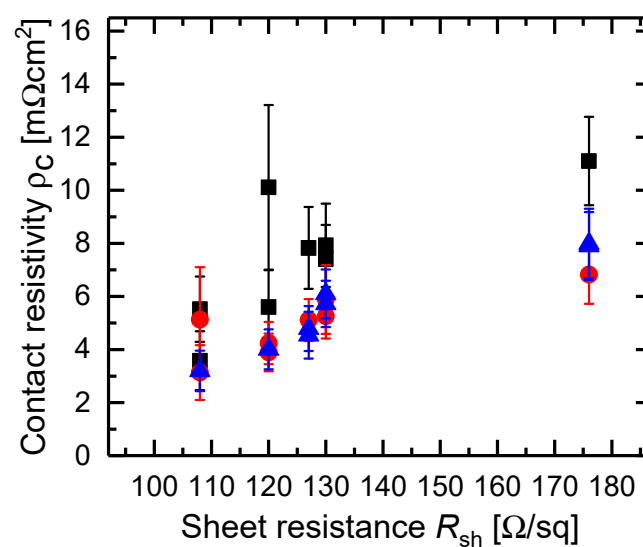


Figure 11. Contact resistivity ρ_C for different sheet resistances R_{sh} of boron laser doped APCVD-layers to screen printed silver paste on three samples (identified by different colors and symbols). The value of ρ_C decreases with decreasing R_{sh} .

3.4. Solar Cell Results

The saturation current density $J_{0,E}$ of the pn-junction influences the electrical characteristics of the solar cell, mainly in terms of the open circuit voltage and therefore, also the efficiency. Clearly, other parameters also have an influence, but they are not considered here. Figure 12 shows the influence of the achieved $J_{0,E}$ on the maximum efficiency of the solar cells by using the support wafers without/with perforation, and without perforation but with SiN. The $J_{0,E}$ was measured on test samples, while solar cells were processed in parallel with the same emitter. The solar cell batches consisted of 10 to 20 cells.

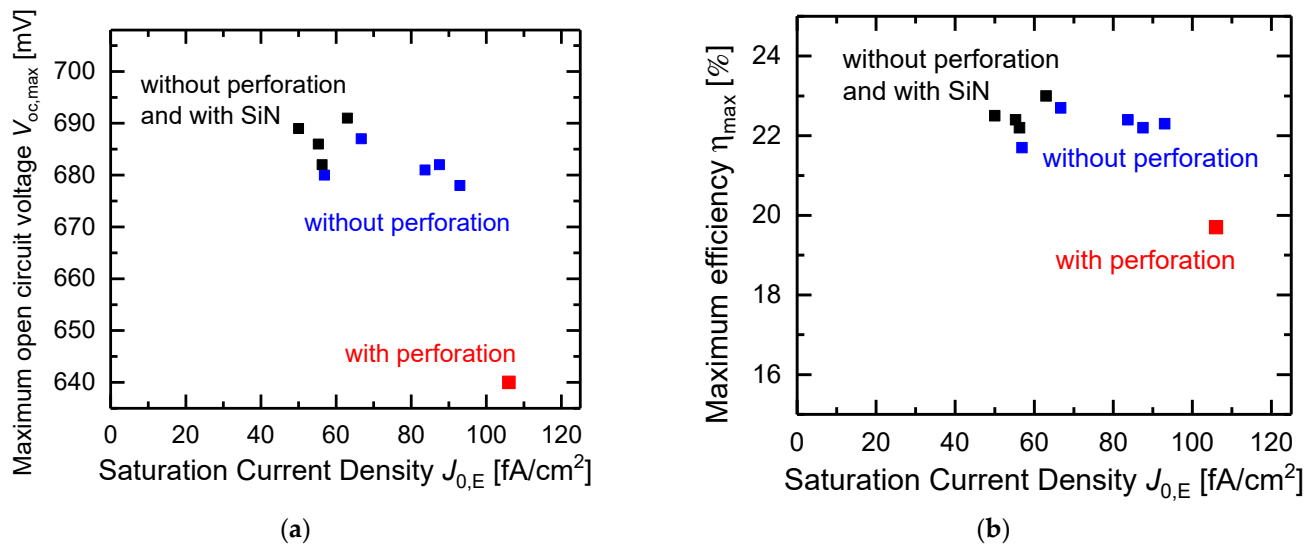


Figure 12. Influence of saturation current density $J_{0,E}$ in solar cell processing on (a) maximum achieved open circuit voltage $V_{oc,max}$ and on (b) maximum achieved efficiency η_{max} . The highest $V_{oc,max}$ and η_{max} is obtained by using support wafers with a SiN barrier layer in the APCVD process for the BSG/USG deposition.

Figure 12a provides the maximum open circuit voltages $V_{oc,max}$ achieved, while Figure 12b presents the maximum efficiencies η_{max} achieved. The highest $V_{oc,max}$ and η_{max} are coupled with the transport by wafers without perforation and with SiN resulting in $V_{oc,max} = 690.7$ mV and $\eta_{max} = 23\%$ —see also Table 1 for the batch with the emitter made of BSG/USG.

With these findings, we processed solar cells with an emitter made of an APCVD layer with a boron concentration of 12%, a thickness of BSG of 40 nm and a thickness of USG of 20 nm, which we deposited on support wafers without perforation and with SiN. Table 1 presents the electrical solar cell parameters of the different batches of solar cells, as follows: efficiencies η with their mean value and standard deviation in the cell batch, maximum achieved efficiency η_{max} , short circuit current density J_{sc} , open circuit voltage V_{oc} , and fill factor FF . The table also compares different processes for boron-emitter formation, including (i) boron laser doping from sputtered boron oxide [16], (ii) boron laser doping from APCVD-layers with BSG and USG, and (iii) the furnace diffusion of boron. Unfortunately, our sputtering equipment did not produce homogeneous boron oxide layers over a large area. Therefore, the cell size for this process was limited to an area $A_{cell} = 4$ cm². Additionally, in contrast to the large area cells $A_{cell} = 244.3$ cm², these small cells did not have screen-printed contacts, but used evaporated aluminium contacts. Table 1 shows that—despite the problem of possible contamination from the metallic belt of the conveyer in the APCVD reactor—the large-area, screen-printed cells with a maximum value of 23% reached close even to our previous best, small-area cells with 23.2% efficiency. Additionally, the results agree with previous data of cells made with the furnace-diffused boron emitter with efficiencies of 23.3%. Therefore, with a high probability, cells with a boron precursor from a commercial APCVD reactor with a ceramic roller transport system might also reach

23.3% if the emitter reaches similar J_{0E} -values such as the $J_{0E,diff} < 40 \text{ fA/cm}^2$ achieved with boron-furnace diffusion. In addition, the overall contact design—which is close to the (old) ZEBRA design of the ISC Konstanz is being reconsidered. The current metallization design used only four bus bars for each polarity on the back side of these cells. Using more busbars would reduce the finger width of the contact fingers and increase the fill factor of the cells.

Table 1. Electrical parameters of the solar cell: efficiency η with the mean value and the mean standard deviation in the cell batch, the maximum achieved efficiency η_{max} together with their values in current density J_{sc} , open circuit voltage V_{oc} and fill factor FF . Comparison is in different cell emitters out of laser doped sputtered boron oxide B_2O_3 , laser doped APCVD-layers and a furnace boron diffusion and cell areas A_{cell} with 4 cm^2 and 244.3 cm^2 . The highest $\eta_{max} = 23.3\%$ reaches the emitter from furnace diffusion because of its higher purity (see Section 2.4). The data were verified with two cells calibrated by ISE CalLab, see Appendix A.

Cell-Emitter	Area $A_{cell} [\text{cm}^2]$	Efficiency η_{max} and η [%]	Current Density $J_{sc} [\text{mA/cm}^2]$	Open Circuit Voltage $V_{oc} [\text{mV}]$	Fill Factor FF [%]
Sputtered B_2O_3 best cell	2×2	23.2	40.1	697.6	82.8
Sputtered B_2O_3 mean (26 cells)	2×2	22.36 ± 0.97	40.28 ± 0.25	694.9 ± 2.5	79.57 ± 3.09
BSG/USG Best cell	244.3	23	41.5	690.7	80.3
BSG/USG mean (13 cells)	244.3	22.63 ± 0.33	41.35 ± 0.12	683.6 ± 7.0	80.04 ± 0.17
Furnace diffused B Best cell	244.3	23.3	41.6	701.4	79.9
Furnace diffused B mean (18 cells)	244.3	23.17 ± 0.07	41.61 ± 0.03	700.4 ± 0.96	79.50 ± 0.23

We also measured the bifaciality of the IBC cells on the module level—see Appendix B. Two modules were assembled out of 120 IBC half cells. The calculation of the bifaciality B according to equation B1 yields $B \approx 70\%$. With a similar metallization scheme, Mihailitchi et al. [30] showed a bifaciality of $B = 67\%$ on the cell level and of $B = 70\%$ on the module level.

4. Absorption in the Precursor Layer

Tailoring the boron-laser doped emitter requires control of the following aspects:

1. Boron concentration C_B of in the BSG;
2. Thickness d_{BSG} of the BSG as the source for laser doping;
3. Thickness d_{USG} of the protecting USG-cap.

Next, we estimated the influence of absorption and reflection in the precursor layer from the results of laser doping (see Section 3.1.4) with the simplification of neglecting interference effects. For laser doping, the laser pulse energy density H_p has to be high enough to melt the Si. Figures 5b and 7b show that the threshold value $H_{p,thres}$ depends on the thickness of the BSG layer. This effect is simply due to the absorption in and also reflection of the BSG and (if too thick) also the USG cap. Doping takes place only if the underlying Si layer melts. Below the threshold energy density, the (parasitic absorption) of the laser pulse in the BSG/USG simply evaporates or ablates the BSG/USG stack but does not yet melt the Si. The data in Figure 5b show that there is no difference in the data for the 20 and 40 nm thick USG layer. Therefore, we neglected the absorption of the laser pulse within these USG layer. Moreover, we ascribed the different threshold values from the data in Figure 7b to parasitic absorption and reflection in the BSG, where the measured threshold energy is higher, because not all of the laser power (and energy) reaches the interface between the BSG and the silicon wafer.

Figure 13a shows the decrease in the laser energy as it passes through the BSG layer. The incident laser energy, if equal to the (measured) threshold energy $H_{p,thres}$, must increase to reach the energy $H_{p,melt}$ which is necessary to melt the Si. From Lambert-Beer's absorption law, we find

$$H_{p,melt}(d_{BSG}) = (1 - R) H_{p,thres} (1 - \exp(-d_{BSG}/L_\alpha)) \quad (5)$$

where L_α stands for the absorption length of the green laser beam within the BSG and R for the reflection of the BSG/USG-layer on top of the Si (which is not shown in Figure 13a).

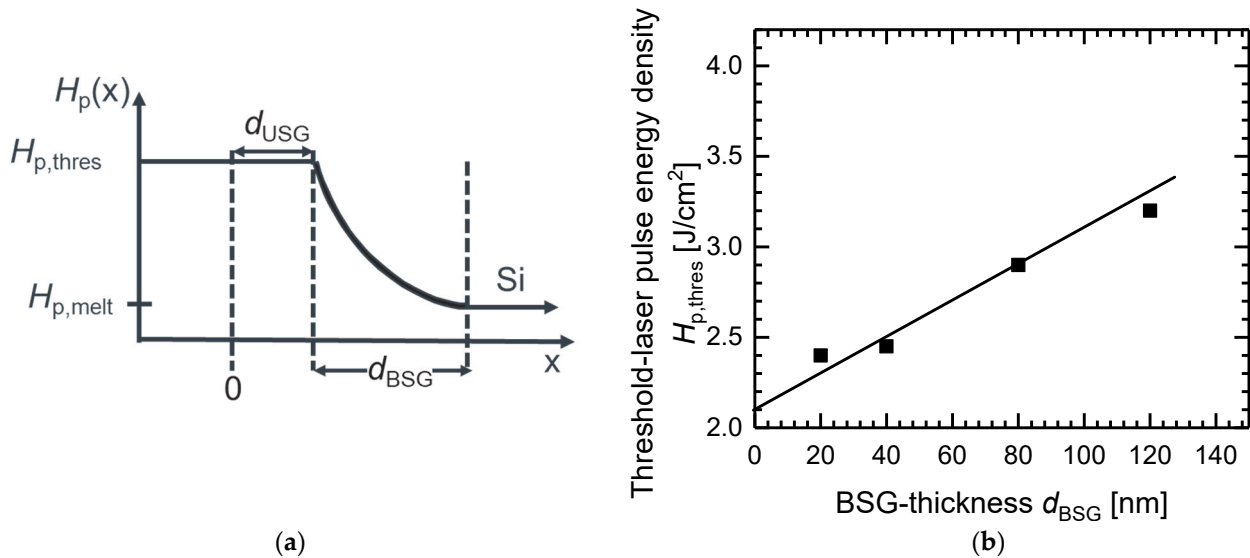


Figure 13. (a) Scheme of the absorbed laser pulse energy density H_p in the APCVD-layer out of BSG and USG. Laser irradiation with H_p hits the surface at $x = 0$, passes the nearly transparent USG and is absorbed by the BSG. Doping takes place only if H_p is high enough for melting Si and exceeds $H_{p,melt}$. (b) As expected from Equation (6), the extracted threshold laser pulse energy density $H_{p,thres}$ out of Figure 7b depends linearly on the BSG-thickness d_{BSG} .

For $d_{BSG} < L_\alpha$, the Taylor expansion of Equation (5) leads to

$$d_{BSG} = L_\alpha / (1 - R) H_{p,melt} / H_{p,thres} \quad (6)$$

where $H_{p,melt}$ equals H_p at $d_{BSG} = 0$ nm (see Equation (5)). As shown in Figure 13b, we can derive an extrapolated value $H_{p,melt} = 2.1$ J/cm² for our laser parameters. This value is in good agreement with our earlier publications [7,8,11,16,20,21] on very thin (around 2 nm) sputtered precursors and supports the assumption that R is approximately independent of the thickness d_{BSG} of the APCVD-deposited layers. Additionally, interference effects in the precursor layer seem to play a minor role.

Finally, Figure 14 plots the thickness of the BSG versus the ratio $H_{p,melt}/H_{p,thres}$. With a measured reflection range of $30\% < R < 40\%$ on different BSG/USG-layers (which is roughly the same reflection as for the polished Si-surface with $R_{Si} = 37\%$), the corrected slope of Figure 14 yields an absorption length in the range $330 \text{ nm} > L_\alpha > 380 \text{ nm}$ for the laser wavelength $\lambda = 532 \text{ nm}$. These large values of the absorption length also justify the use of the Taylor expansion in Equation (6).

Our value of an absorption length of around $0.4 \mu\text{m}$ is surprising because the literature data for silicate glasses indicate low absorption (and therefore higher absorption lengths) in this wavelength regime. However, Kitamura et al. [31] stated in their review that silica glasses differ in their optical properties due to "the silica glass synthesis method, composition, impurity, and defects level, sample thickness, surface roughness, and temperatures as well as the retrieval method". If we consider the glass-formation temperature of borosilicate

glass of around 460 °C [32] and our lower deposition temperatures of 400 °C, we speculate that, in our case, more transparent “glass” had not yet formed. This could explain the difference between the literature data for the absorption of borosilicate glass and the data of our deposited BSG and USG. Additionally, Heilig et al. [14] stated that laser doping from as-deposited (like we did) APCVD layers results in higher doping than laser doping with thermally treated glasses. Clearly, this aspect of laser doping from the APCVD layers deserves more detailed optical study. In particular, a comparison of the optical properties of the APCVD-deposited BSG layers which underwent different thermal treatments requires future investigation. A comparison with BSG-layers from furnace diffusion in future studies will prove interesting. Such basic research was not the primary focus of our present work which concentrated on the basic technologies for processing industrial Laser-IBC solar cells.

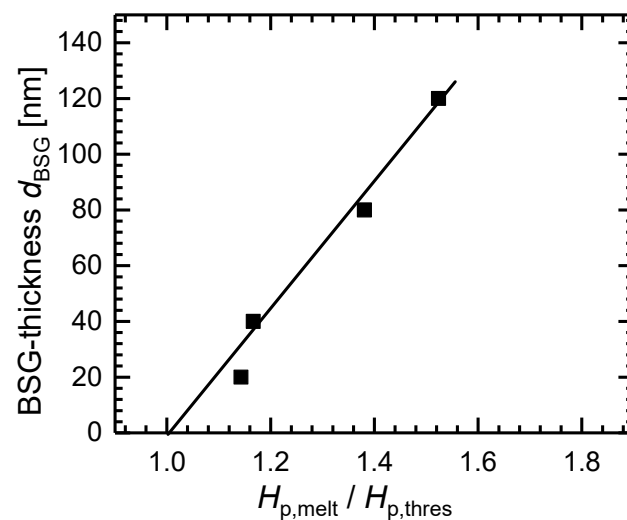


Figure 14. Linear dependence of BSG-thickness d_{BSG} and the relation of the threshold pulse energy densities $H_{p,melt}/H_{p,thres}$. Using Equation (6) and $R = 0$, the slope yields an (uncorrected) $L_{\alpha} = 230$ nm at the laser wavelength $\lambda = 532$ nm. Considering the measured reflections $30\% < R < 40\%$ yields corrected absorption lengths $330 \text{ nm} < L_{\alpha} < 380$ nm.

5. Conclusions

Boron-containing precursors derived from an APCVD process are well suited for the fabrication of industrial IBC solar cells using laser doping. For large-area cells, we reached an efficiency of up to 23%. According to our experiments with different carrier wafers, this efficiency value is likely to be limited by impurities which, most probably, stem from the metallic belt, which is used in the conveyer system of the lab-type APCVD system. Avoiding this contamination, with the use of, for example, a commercial APCVD system with a ceramic roller-transport system, could lead to an efficiency similar to that of solar cells with furnace-diffused emitters of 23.3%.

For the safe transport of the deposited APCVD layer between different lab locations, a protected nitrogen atmosphere is needed. Under such protection, the precursors can survive for up to three weeks.

In the past, we used only several-nanometer thick, sputtered precursors for boron laser doping IBC solar cells. For such thin layers, the absorption and reflection of the laser beam within the precursor plays no role. The APCVD-deposited layers used here were much thicker. In this case, one must consider parasitic absorption and reflection within the precursor itself. For the green laser beam of a $\lambda = 532$ nm wavelength, we observed an absorption length in the range of $380 \text{ nm} < L_{\alpha} < 330$ nm for the BSG with a boron concentration of 12%.

Author Contributions: Conceptualization, R.Z.-G. and J.H.W.; methodology, R.Z.-G., V.M. and S.F.-R.; validation, R.Z.-G. and T.B.; formal analysis, R.Z.-G. and J.H.W.; investigation, S.F.-R., M.S., E.-P.W. and M.H.; resources, J.K., R.K., J.H.W. and S.S.; data curation, S.F.-R., M.S., E.-P.W., T.B., M.H. and S.S.; writing—original draft preparation, R.Z.-G. and J.H.W.; writing—review and editing, R.Z.-G. and J.H.W.; visualization, R.Z.-G.; supervision, R.Z.-G. and J.H.W.; project administration, R.Z.-G.; funding acquisition, R.Z.-G. and J.H.W. All authors have read and agreed to the published version of the manuscript.

Funding: This work was funded by the German Federal Ministry of Economics and Technology (BMWi) project No. 0324212 and Energy Baden-Württemberg (EnBW).

Informed Consent Statement: Informed consent was obtained from all subjects involved in the study.

Acknowledgments: We thank E. Hoffmann for fruitful discussions during the processing of solar cells and M. Saliba for the opportunity to record the results at *ipv* and for support in the BMWi project. We also gratefully acknowledge the experimental support of the *ipv*-technology group under the leadership of B. Winter. We are also grateful for the production and measurements of the solar modules by Ingo Ullmann from ISC Konstanz. Finally, we thank the reviewers for their careful reading of the manuscript which helped to improve our text.

Conflicts of Interest: The authors declare no conflict of interest.

Appendix A

Our in-house measurements, shown in Table 1, were performed with a sun simulator under standard test conditions. Table A1 shows a comparison with the calibration measurements at ISE CalLab on two IBC cells. The values of our in-house measurements are within the error limits of the calibration measurements of ISE CalLab.

Table A1. Electrical parameters of the solar cells calibrated at ISE CalLab in comparison to our in-house measurements at Standard Test Conditions: efficiency η , current density J_{sc} , open circuit voltage V_{oc} and fill factor FF . Efficiency values of our measurements and from ISE CalLab are in the limit of error.

Cell	Area A_{cell} [cm ²]	Efficiency η [%]	Short Circuit Current Density J_{sc} [mA/cm ²]	Open Circuit Voltage V_{oc} [mV]	Fill Factor FF [%]
Cell 1, in-house	244.3	22.4	41.1	682.7	79.8
Cell 1, ISE	244.3	22.32 ± 0.34	40.83	682.9	80
Cell 2, in-house	244.3	22.4	41.4	685.8	79
Cell 2, ISE	244.3	22.24 ± 0.34	41.19	684.5	78.9

Appendix B

The determination of the bifaciality of our IBC cells was performed on the module level. We assembled two modules, each containing 120 half cells. An h.a.l.m. module flasher AAA type with a 1 × Xenon lamp cetisPV-CT had the characteristic values of the power $P_{MPP,mod}$ at the maximum power point, efficiency η_{mod} , short circuit current $I_{sc,mod}$, open circuit voltage $V_{oc,mod}$, and fill factor FF_{mod} . Table A2 shows the values of two different modules and the calculated bifaciality.

$$B = \eta_{mod,rear} / \eta_{mod,front} \quad (A1)$$

where $\eta_{mod,rear}$ is the efficiency measured with the illumination from the rear side and $\eta_{mod,front}$ is the illumination from the front side of the module. Module 1 shows $B_1 = 0.692$ and module 2 has $B_2 = 0.724$.

Table A2. Electrical parameters of the modules made out of 120 IBC half cells with given mean values out of five measurements and their standard deviation. Illumination occurs either from the front side or the rear side of the modules. The Bifaciality B was calculated using Equation (A1).

Module	MPP Power $P_{MPP,mod}$ [W]	Efficiency η_{mod} [%]	Short Circuit Current $I_{sc,mod}$ [A]	Open Circuit Voltage $V_{oc,mod}$ [V]	Fill Factor FF_{mod} [%]
Front: Module 1—mean	323.4	19.45	10	42.03	76.93
Front Module 1—st. dev.	0.1163	0.0069	0.0018	0.0084	0.035
Rear: Module 1—mean	223.7	13.45	7.016	41.09	77.61
Rear: Module 1—st. dev.	0.07	0.0042	0.0022	0.0018	0.022
Bifaciality B : Module 1	0.692	0.692			
Front: Module 2—mean	305.8	18.38	9.68	40.79	77.47
Front Module 2—st. dev.	0.156	0.0094	0.0032	0.0159	0.04
Rear: Module 2—mean	216.4	13.01	7.006	40.03	77.17
Rear: Module 2—st. dev.	0.064	0.0038	0.003	0.0108	0.0367
Bifaciality B : Module 2	0.724	0.724			

References

1. Monthly TaiyangNews Update on Commercially Available High Efficiency Solar Modules. Available online: <https://taiyangnews.info/top-modules/top-solar-modules-listing-april-2022/> (accessed on 16 May 2022).
2. Smith, D.; Cousins, P.; Westerberg, S.; De Jesus-Tabajonda, R.; Aniero, G.; Shen, Y.-C. Toward the Practical Limits of Silicon Solar Cells. *IEEE J. Photovolt.* **2014**, *4*, 1465–1469. [CrossRef]
3. Cousins, P.; Smith, D.; Luan, H.; Manning, J.; Dennis, T.; Waldhauer, A.; Wislon, K.; Harley, G.; Mulligan, W. Generation 3: Improved performance at lower cost. In Proceedings of the 2010 35th IEEE Photovoltaic Specialists Conference, Honolulu, HI, USA, 20–25 June 2010; pp. 000275–000278.
4. Smith, D.D.; Cousins, P.J.; Masad, A.; Westerberg, S.; Zhu, X.; Meyers, B.; Bourne, B.; Shields, M.; Rose, D.; Bergstrom, N. SunPower’s Maxeon Gen III solar cell: High efficiency and energy yield. In Proceedings of the 2013 IEEE 39th Photovoltaic Specialists Conference (PVSC), Tampa, FL, USA, 16–21 June 2013; pp. 0908–0913.
5. Green, M.A.; Dunlop, E.D.; Hohl-Ebinger, J.; Yoshita, M.; Kopidakis, N.; Hao, X. Solar cell efficiency tables (Version 58). *Prog. Photovolt. Res. Appl.* **2021**, *29*, 657–667. [CrossRef]
6. Dahlinger, M.; Bazer-Bachi, B.; Röder, T.C.; Köhler, J.R.; Zapf-Gottwick, R.; Werner, J.H. Laser-Doped Back-Contact Solar Cells. *IEEE J. Photovolt.* **2015**, *5*, 812–818. [CrossRef]
7. Dahlinger, M.; Bazer-Bachi, B.; Röder, T.C.; Köhler, J.R.; Zapf-Gottwick, R.; Werner, J.H. 22.0% Efficient laser doped back contact solar cells. *Energy Procedia* **2013**, *382*, 50–253. [CrossRef]
8. Köhler, J.R.; Grabitz, P.; Eisele, S.J.; Röder, T.C.; Werner, J.H. Laser doped selective emitters yield 0.5% efficiency gain. In Proceedings of the 24th EUPVSEC, Hamburg, Germany, 17–22 September 2009; pp. 1847–1850.
9. Weber, J.; Gutscher, S.; Lohmüller, S.; Brand, A.A. Laser-doped selective emitter—Process development and speed-up. In Proceedings of the 35th EUPVSEC, Brussels, Belgium, 24–28 September 2018; pp. 379–384.
10. Pengcheng, Q.; Pengxiang, Q. Characteristics and development of interdigital back contact solar cells. *IOP Conf. Ser. Earth Environ. Sci.* **2021**, *621*, 012067. [CrossRef]
11. Dahlinger, M.; Carstens, K.; Hoffmann, E.; Zapf-Gottwick, R.; Werner, J.H. 23.2% laser processed back contact solar cell: Fabrication, characterization and modeling. *Prog. Photovolt. Res. Appl.* **2017**, *25*, 192–200. [CrossRef]
12. Rothhardt, P.; Demberger, C.; Wolf, A.; Biro, D. Co-diffusion from APCVD BSG and POCl₃ for industrial n-type solar cells. *Energy Procedia* **2013**, *38*, 305–311. [CrossRef]
13. Meier, S.; Wiesnet, S.; Mack, S.; Werner, S.; Maier, S.; Unmüßig, S.; Demberger, C.; Knauss, H.; Biro, D.; Wolf, A. Co-Diffusion for p-type PERT solar cells using APCVD BSG layers as Boron doping source. In Proceedings of the 32nd EUPVSEC, Munich, Germany, 20–24 June 2016; pp. 20–24.
14. Heilig, M.; Engelhardt, J.; Hahn, G.; Terheiden, B. Comparison of Laser-Doped Emitters from As-Deposited and Thermally Diffused APCVD Doping Glasses on Silicon Substrates. *AIP Conf. Proc.* **2019**, *2147*, 070004. [CrossRef]
15. Kern, W.; Puotinen, D. Cleaning Solutions Based on Hydrogen Peroxide for Use in Silicon Semiconductor Technology. *RCA Rev.* **1970**, *31*, 187.
16. Dahlinger, M.; Carstens, K. Optimized laser doped back surface field for IBC solar cells. *Energy Procedia* **2016**, *92*, 450–456. [CrossRef]
17. Kopecek, R.; Libal, J.; Lossen, J.; Mihailtchi, V.D.; Chu, H.; Peter, C.; Buchholz, F.; Wefringhaus, E.; Halm, A.; Ma, J.; et al. ZEBRA technology: Low cost bifacial IBC solar cells in mass production with efficiency exceeding 23.5%. In Proceedings of the 2020 47th IEEE Photovoltaic Specialists Conference (PVSC), Virtual meeting, 15 June–21 August 2020; pp. 1008–1012.

18. Galbiati, G.; Chu, H.; Mihaietchi, V.D.; Libal, J.; Kopecek, R. Latest Results in Screen-Printed IBC-ZEBRA Solar Cells. In Proceedings of the IEEE 7th World Conference on Photovoltaic Energy Conversion (WCPEC), Hilton Waikoloa Village Resort, HI, USA, 10–15 June 2018; pp. 1540–1543.
19. Sinton, R.A.; Cuevas, A.; Stuckings, M. Quasi-Steady-State Photoconductance, A New Method for Solar Cell Material and Device Characterization. In Proceedings of the 25th IEEE Photovoltaic Specialists Conference, Washington, DC, USA, 13–17 May 1996; pp. 457–460.
20. Hassan, M.; Dahlinger, M.; Köhler, J.R.; Zapf-Gottwick, R.; Werner, J.H. Unified Model for Laser Doping of Silicon from Precursors. *Materials* **2021**, *14*, 2322. [[CrossRef](#)] [[PubMed](#)]
21. Köhler, J.; Eisele, S. Influence of precursor layer ablation on laser doping of silicon. *Prog. Photovolt: Res. Appl.* **2010**, *18*, 334–339. [[CrossRef](#)]
22. Eisele, S. Laser Doping of Silicon Solar Cells. Ph.D. Thesis, University of Stuttgart, Stuttgart, Germany, 2011.
23. Available online: <http://SCHMID-group.com/en/business-units/thermal-processing/apcvd-system/#Benefits> (accessed on 15 May 2021).
24. Liehr, M.; Lewis, J.E.; Rubloff, G.W. Kinetics of high-temperature thermal decomposition of SiO₂ on Si (100). *J. Vac. Sci. Technol. A Vac. Surf. Films* **1987**, *5*, 1559–1562. [[CrossRef](#)]
25. Blum, A.L.; Swirhun, J.S.; Sinton, R.; Kimmerle, A. An Updated Analysis to the WCT-120 QSSPC measurement system using advanced device physics. In Proceedings of the 28th European Photovoltaic Solar Energy Conference and Exhibition, Paris, France, 30 September–4 October 2013; pp. 1521–1523.
26. Kimmerle, A.; Rothhardt, P.; Wolf, A.; Sinton, R.A. Increased reliability for J₀-analysis by QSSPC. *Energy Procedia* **2014**, *55*, 101–106. [[CrossRef](#)]
27. Cuevas, A. The effect of emitter recombination on the effective lifetime of silicon wafers. *Sol. Energy Mat. Sol. Cells* **1999**, *57*, 277. [[CrossRef](#)]
28. Ametowobla, M. Characterization of a Laser Doping Process for Crystalline Silicon Solar Cells. Ph.D. Thesis, University of Stuttgart, Stuttgart, Germany, 2010.
29. Min, B.; Dastgheib-Shirazi, A.; Altermatt, P.P.; Kurz, H. Accurate determination of the emitter saturation current density for industrial P-diffused emitters. In Proceedings of the 29th EUPVSEC, Amsterdam, The Netherlands, 22–26 September 2014; pp. 463–466.
30. Mihaietchi, V.; Halm, A.; Chu, H.; Libal, J.; Kopecek, R.; Jikui, M.; Jianda, L.; Yonggang, G.; Peng, D. Bifacial IBC (ZEBRA) Technology. In Proceedings of the 6th BifIPV Workshop, Amsterdam, The Netherlands, 31 March–1 April 2019.
31. Kitamura, R.; Pilon, L.; Jonasz, M. Optical constants of silica glass from extreme ultraviolet to far infrared at near room temperature. *Appl. Opt.* **2007**, *46*, 8118. [[CrossRef](#)] [[PubMed](#)]
32. Avramov, I.; Vassilev, T.; Penkov, I. The glass transition temperature of silicate and borate glasses. *J. Non-Cryst. Solids* **2005**, *351*, 472–476. [[CrossRef](#)]